CHEMISTRY OF MATERIALS

pubs.acs.org/cm

Article

Synthesis of Embryonic Zeolites with Controlled Physicochemical Properties

Mariame Akouche, Jean-Pierre Gilson, Nikolai Nesterenko, Simona Moldovan, Daniel Chateigner, Hussein El Siblani, Delphine Minoux, Jean-Pierre Dath, and Valentin Valtchev*

Cite This: https://dx.doi.org/10.1021/acs.chemmater.9b05258

Read Online

ACCESS | Metrics & More | Article Recommendations | Supporting Information

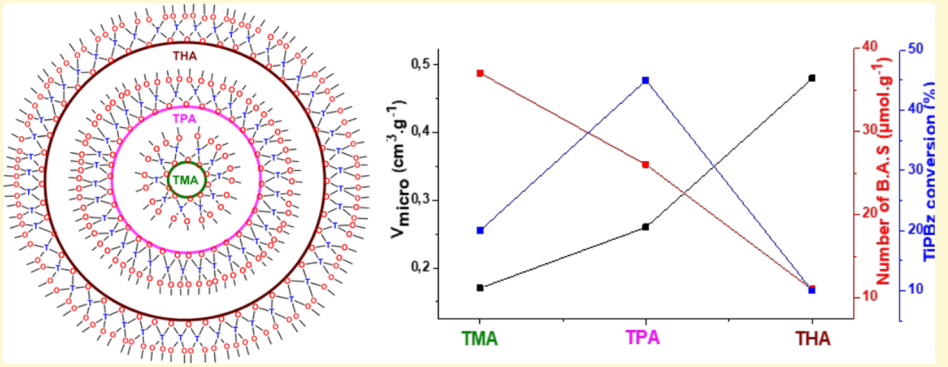

ABSTRACT: Colloidal zeolite precursors with sharp particle size distributions (ca. 3−5 nm) and identical chemical compositions, so called embryonic zeolites (EZs), are prepared by strict control of aluminosilicate precursor polymerization in zeolite-yielding systems. The organic structure-directing agent (OSDA) acts as a sacrificial template and is eliminated by high-temperature combustion after the synthesis. Physicochemical properties of the EZs, such as the pore size and volume and specific surface area, are determined by the size of the OSDA and synthesis conditions employed, that is, the larger the OSDA, the higher the microporous volume and the specific surface area of the derived EZs. The EZs belong to the family of extra-large microporous (1−2.5 nm) materials. Upon calcination, EZs retain their structure/porosity, and most of their aluminum remains in a tetrahedral coordination to provide Brønsted acidity. Pyridine adsorption shows a lower acidic strength for embryonic zeolites with respect to their crystalline counterparts (zeolites). An appropriate combination of extra-large micropores (1−2.5 nm) and Brønsted acid sites (~25 μmol·g^{-1}) leads to improved catalytic performances in the dealkylation of TiPBz, a proxy for bulky molecules reacting only on the external surface of crystalline zeolites. By varying the size of the OSDA for synthesizing the EZ, materials with controlled porosity, acidity, accessibility, and catalytic activity are prepared, and their properties extend to existing crystalline zeolites.

INTRODUCTION

Molecular sieve zeolites are widely used as heterogenous catalysts in a variety of industrial (oil refining, petro-, and fine chemicals production) and environmental (exhaust gas treatment, heavy and radioactive ion sequestration, ...) applications.[1,2] They typically offer high surface areas, uniform micropores with well-defined topology, strong acid sites, and high thermal and chemical stability.[3−5] A unique property of zeolite materials is their shape selectivity,[3] which is a consequence of their active sites being confined in well-defined micropore spaces. However, the presence of such micropores often imposes transport limitations on reactants and products, in particular, those with a size close to or larger than the pore diameter.[5] These steps become rate-determining in the catalytic activity, and the full potential of theses catalysts is not reached. In the case of bulky molecules larger than zeolite pores, the only accessible and active sites are those located on the outer surface of the crystals and their pore openings.

In summary, the problems of diffusion and related low accessibility to the active sites represent a major roadblock in a number of industrial reactions catalyzed by zeolites (cracking, oxidation, esterification, ...). To meet exacting industrial requirements,[6] much effort is devoted to preparing zeolite materials with better accessibility and improved transport properties. The most explored avenues to improve catalytic performances were focused on decreasing zeolite crystal size[7−11] and preparing zeolites containing a system of larger

Received: December 19, 2019
Revised: February 3, 2020
Published: February 4, 2020

(meso-)pores.[12−17] A mesoporous network connected to the native micropores in zeolite crystals decreases mass transport limitations, but it does not affect the limited intrinsic ability of zeolites to process bulky molecules. Both solutions, nanozeolites and mesopore-containing zeolites, bear some limitations; in particular, the active sites in the zeolite channels remain inaccessible for bulky molecules, and therefore alternative solutions are required.

Recently, we addressed this issue by preparation of zeolite units with sizes of few nanometers.[18] These units denoted "embryonic zeolites" exhibit only a short-range order and comprise elements of zeolite structure. Their semi-formed unit cells offer easier access of much bulkier molecules to the active sites than that of their fully crystalline counterparts, which exhibit a long-range order. The embryonic zeolites were prepared as a monodisperse suspension containing nanoparticles that are uniform in size and composition.[18] They exhibit superior catalytic activity with respect to the fully crystalline material (zeolite) synthesized from the same initial system.

For instance, embryonic zeolites synthesized with tetrapropylammonium as a structure-directing agent exhibit pores in the range of 1−2 nm. The extension of zeolite pore size to 1−2 nm would allow us to process much bulkier molecules than the "current" available zeolites can process. At present, only Ge-silicate zeolites exhibit pores larger than 1 nm,[19] while the conventional alumino-silicate zeolites are limited to 1 nm in pore size. Unfortunately, the limited (hydro)thermal stability of Ge-silicate zeolites so far precluded their commercial use. Thus, the quest for extra-large-pore zeolitic materials continues to be a topic of high priority. Here, we address this issue by preparation of a few nanometer-large zeolitic nanounits that offer full accessibility to their active sites by relaxing diffusion limitations.

Sacrificial organic templates are commonly used in the synthesis of nanoporous materials.[20,21] In the synthesis of zeolitic materials, the organic template, often called the organic structure-directing agent (OSDA), plays a key role in the formation of zeolite structure and charge distribution in the framework.[19] In general, these are positively charged molecules that balance the negative charge introduced by Al cations in the zeolite framework. Each OSDA has a fixed size/charge ratio; therefore, the total guest volume is determined by the number of guest molecules that will correspond to the framework charge density.[22−24]

The objective of this study is the preparation of embryonic zeolites with pores exceeding 1 nm with a few-nanometer particle size and controlled pore size and pore volume. A series of tetraalkylammonium (TAA^+) cations with sizes ranging between 6 and 12 Å were employed. The series includes: tetramethylammonium (TMA^+), tetrapropylammonium (TPA^+), trimethyladamantylammonium ($TMAd^+$), tetrabutylammonium (TBA^+), and tetrahexylammonium (THA^+). With the exception of THA^+, which is too big to yield a zeolite-type microporous material, all other OSDAs generate zeolite structures.[25] Embryonic zeolites with different micropore volumes and specific surface areas are obtained. Their catalytic activities are evaluated in the dealkylation of a model molecule, 1,3,5-triisopropylbenzene (1,3,5-TiPBz) hardly penetrating the micropores of any industrially relevant zeolite. It is, therefore, commonly used to study the external surface properties of zeolites, including those with large pores.[26,27]

EXPERIMENTAL SECTION

Preparation of Embryonic Precursors. All syntheses started from clear homogeneous sols with a molar composition of $9OSDA{:}0.25Al_2O_3{:}25SiO_2{:}430H_2O{:}100EtOH$ where OSDA can be tetramethylammonium hydroxide (TMA·OH 25% in water, Alfa Aesar), tetrapropylammonium hydroxide (TPA·OH 20% in water, Alfa Aesar), trimethyladamantylammonium hydroxide (TMAd·OH 25% in water, Sachem), tetrabutylammonium hydroxide (TBA·OH 40% in water, Alfa Aesar), and tetrahexylammonium hydroxide (THA·OH 20% in water, Sigma-Aldrich). After mixing the OSDA with distilled water, aluminum sulfate (98%), and tetraethylorthosilicate (TEOS 98%), the solution was hydrolyzed at room temperature for 6 h in a closed polypropylene bottle. The complete hydrolysis was confirmed by the appearance of a clear monophasic solution. Then, this solution was either dried by freeze-drying at −94 °C under vacuum (to avoid any further crystallization) or hydrothermally treated at 90 °C for 12, 15, 18, 144, and 216 h as the kinetics of the synthesis depends on the nature of the OSDA. After the synthesis, the solid was recovered by freeze-drying and further calcined at 550 °C for 5 h in a static oven under air.

The following series of zeolite precursor (P) samples were prepared by:

(1) Room temperature synthesis (P_{RT}): P_{RT}-TMA, P_{RT}-TPA, P_{RT}-TBA, P_{RT}- TMAd, and P_{RT}-THA.
(2) Hydrothermal synthesis: $P_{x\text{-}y}$-SDA where x is the temperature in degree Celsius and y is the crystallization time in hours, for example, $P_{90\text{-}15}$-TMA, $P_{90\text{-}216}$-TMAd, ...

A highly crystalline nanosized ZSM-5 prepared from the same initial suspension (P-TPA) at 100 °C for 48 h was used as a reference sample.

Characterization. All materials were characterized by powder X-ray diffraction (PXRD) using a PANalytical X'Pert Pro diffractometer with average Cu Kα radiation (λ = 1.5418 Å). We used a θ−2θ scan in the 3°−50° 2θ range and a 0.02° step. The whole pattern was fitted using the combined analysis formalism[28] implemented in the MAUD program,[29] a type of software using an extended Rietveld[30] analysis approach. Since severe line broadening was observed in the diffraction diagrams, we analyzed those within the combined analysis approach. The instrumental contribution to the line broadening was calibrated on LaB6 srm660b standard powder from the National Institute of Standards and Technology. The Popa[31] formalism was then used to describe anisotropic crystallite sizes and shapes. No preferred orientation was detected during the fit. The ZSM5 structural model no. 1505105 from the Crystallography Open Database[32] was used as a starting model in the refinement.

Nitrogen adsorption measurements were carried out on a Micromeritics ASAP 2020 surface area analyzer. The calcined samples were analyzed after degassing at 300 °C. The isotherms were recorded using the ASAP 2020 analysis program. The microporous volume (V_{mic}, $cm^3{\cdot}g^{-1}$) and external surface area (S_{ext}, $m^2{\cdot}g^{-1}$) were obtained from the t-plot method based on the Harkins−Jura equation. The macro- and mesopore size distribution was obtained from the desorption branch using the Barrett Joyner Halenda algorithm assuming cylindrical pores. For refined analysis, the micro-mesopore size distribution was extracted from density functional theory modeling of the adsorption branch. TG-DSC measurements of different samples were carried out on a SETSYS evolution instrument (SETARAM). Approximately 10 mg of each sample was introduced in an alumina crucible that is loaded in the analyzer chamber. The sample was heated from 30 to 800 °C with a heating ramp of 5 °C·min^{-1} under air (flow rate: 40 mL·min^{-1}).

All NMR measurements were done with 4 mm (o.d.) zirconia rotors and with a spinning speed of 12 kHz. The solid-state $\{^1H\}$ -^{13}C CP-MAS NMR spectra were recorded on a Bruker Avance 400 spectrometer operating at 100.6 MHz. During the pulse program, a $\pi/2$ pulse of 3.7 μs on ^1H, contact time of 2 ms, and recycle delay of 2 s were used. ^{27}Al MAS NMR was recorded on a Bruker Avance 500 spectrometer operating at 130.3 MHz. ^{27}Al MAS NMR was obtained with a $\pi/12$ pulse and recycle delay of 1 s. The amount of

https://dx.doi.org/10.1021/acs.chemmater.9b05258
Chem. Mater. XXXX, XXX, XXX−XXX

nontetrahedral Al was estimated by the integration of the peak area using a Dmfit program. The results were verified by the Top Spin program. The solid-state ^{29}Si NMR (1 pulse) spectrum was also recorded on a Bruker Avance III-HD 500 spectrometer (11.7 T) operating at 99.3 MHz using zirconia rotors of 4 mm in outer diameter spun at 12 kHz. A single-pulse excitation (30° flip angle) is used with a recycle delay of 30 s. TMS was the reference for ^{29}Si and ^{13}C, while a 1 M $Al(NO_3)_3$ solution was used for ^{27}Al. ^{129}Xe NMR experiments were performed on a Bruker AV III 400 wide-bore spectrometer equipped with a 10 mm BBO probe, operating at a frequency of 110.64 MHz for ^{129}Xe. Prior to each experiment, the sample was introduced into a home-designed (10 mm o.d.) NMR tube and dehydrated under high vacuum overnight at 413 K. The hyperpolarized (HP) ^{129}Xe gas was obtained using a home-built xenon polarizer based on the spin-exchange optical pumping (SEOP) technique.[33,34] HP ^{129}Xe NMR spectra were acquired under a continuous recirculating flow of 50 mL·min^{-1} of a gas mixture containing 4% Xe, 6% N_2, and 90% He at a total absolute pressure of 1.5 bar. For all variable-temperature (VT) measurements and after each temperature change performed at a speed of 5 K·min^{-1}, a delay of ∼20 min was generally necessary to ensure a homogeneous temperature all over the sample, and this stability was checked by directly monitoring the xenon chemical shifts. All spectra were referenced to free xenon gas at 0 ppm. The IR spectra were recorded on a Shimadzu IR Affinity-1 Fourier transform infrared spectrophotometer using the KBr pellet technique. Pyridine and collidine adsorption were used to evaluate the acidity and accessibility of the samples. The study was performed using a standard in situ FTIR setup. Infrared spectra were recorded on a Nicolet Magna 550 FTIR spectrometer equipped with a DTGS detector at a 4 cm^{-1} optical resolution with one level of zero filling for the Fourier transform. Prior to measurement, the sample was grinded and pressed into a self-supporting disc (diameter: 2 cm, approximately 5 mg·cm^{-2}) and activated in vacuum (ca. 10^{-6} hPa) at 460 °C for 2 h at 2 °C·min^{-1}. After cooling to room temperature, the spectrum of the sample was recorded for further use as a reference. Then, a pressure of 1.33 hPa of the probe molecule (P.M.) was established in the cell at an ambient temperature to reach saturation. The wafer was heated at 100 °C for 15 min to facilitate diffusion of the P.M. into the sample. Successive evacuations were performed at 25, 50, 100, 150, 200, 250, 300, and 350 °C at 15 min intervals. All spectra were normalized to a 2.5 mg·cm^{-2} wafer. The amounts of acidic sites were determined using the areas of the bands at 1450 cm^{-1} (Lewis) and 1545 cm^{-1} (Brønsted) in the case of pyridine adsorption and at 1644 cm^{-1} (Brønsted) in the case of collidine adsorption. The molar extinction coefficients (ε) used for quantification were ε1545 (B-pyridine) = 1.8 cm·μmol^{-1}, ε1455 (L-pyridine) = 1.5 cm·μmol^{-1} and ε1644 (B-collidine) = 10.1 cm·μmol^{-1}.[35] The OMNIC version 7.3 SP1 program was used for data processing.

The transmission electron microscopy (TEM) investigations were carried out on a double-corrected cold FEG Jeol ARM Analytical transmission electron microscope. Due to the materials' high sensitivity to electron beam irradiation, an accelerated voltage of at 80 kV was employed, and the micrographs were acquired under the scanning TEM (STEM) mode using the high-angular annular dark field (HAADF) detection methodology. In this approach, a 0.1 nm diameter beam scanned the region of interest, and the image was recorded at a camera length of 8 cm and in the semi-angular range of 70−280 mrad. Size-calibrated Au nanoparticles were employed for the STEM fine alignments. The images were acquired at a speed of 12 μs·px^{-1} for image sizes of 1024 × 1024 px using the Digiscan Plugin implemented in the Digital Micrograph software. A few drops of an ethanol-based solution containing the specimens dispersed in ethanol and with which ultrasound was used were deposited on a holey carbon membrane disposed on 300 mesh Cu grids.

Catalytic Testing. The catalytic performances were evaluated in the dealkylation of 1,3,5-triisopropylbenzene (TiPBz) in a down-flow atmospheric reactor. In a typical catalytic test, 20 mg of the catalyst (dry mass) was loaded at the center of a stainless-steel tubular reactor (internal diameter of 1/2″) and activated in situ at 460 °C (ramping from room temperature at 5 °C·min^{-1}) under a dry air flow (50 mL·min^{-1}) for 1 h. The temperature was subsequently lowered to 300 °C under a nitrogen flow (50 mL·min^{-1}). The nitrogen flow was then diverted to a saturator (operated at 70 °C) filled with TiPBz (Alfa Aesar, 97%), generating a TiPBz partial pressure of 170 Pa feeding the reactor. The WHSV (weight hourly space velocity) was held constant at 8 h^{-1} for all tests. The conversions were measured at 300 °C over 100 min. The online analysis of the products and unconverted reactant, transferred via a line heated at 150 °C to a gas sampling valve, was monitored by a Varian CP-3800 gas chromatograph equipped with a flame ionization detector (FID) and a HP-PONA cross-linked methyl siloxane column, 50 m (L) × 0.2 mm (i.d.) × 0.5 μm (film thickness). The temperature of the column was kept at 160 °C throughout the measurement. The injection temperature was maintained at 200 °C, while the detection temperature was maintained at 250 °C.

RESULTS AND DISCUSSION

Discrete nanometer-sized embryonic zeolites can only be obtained if the polymerization between silica and alumina precursor species and the OSDA is closely controlled to avoid the formation of large and dense gel particles with various sizes and compositions. This is also a necessary condition to assess their physicochemical properties. Such a general rule is particularly important with amorphous materials lacking a long-range structural order. Optically clear sols containing only discrete gel particles are therefore used in all our syntheses to harvest solids with similar sizes, compositions, and porosities.

Impact of the OSDA on the Physicochemical Properties of Embryonic Zeolites. Alkylammonium cations of varying sizes acting as organic structure-directing agents (OSDAs) allow studying the properties of the porous solids harvested from syntheses performed at room temperature (RT). After complete hydrolysis of the silica source (TEOS), the resulting samples are freeze-dried and characterized.

According to DLS, all precursor sols present a monomodal particular size distribution with a size between 1 and 10 nm, Figure 1. The size of embryonic zeolites depends on the size of

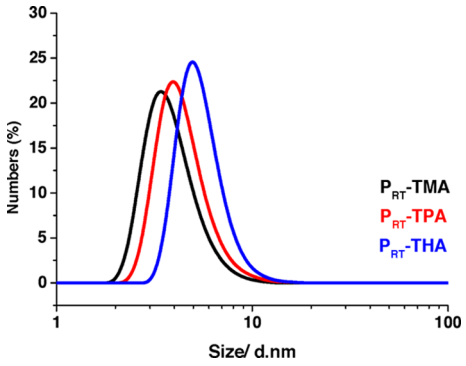

Figure 1. Particle size distribution of P_{RT}-TMA, P_{RT}-TPA, and P_{RT}-THA suspensions.

the template employed, and a clear relation is observed: maxima in the DLS peaks of P_{RT}-TMA, P_{RT}-TPA, and P_{RT}-THA are 2, 3, and 4.5 nm, respectively. The synthesis conditions are such that no material exhibits any long-range structural order, monitored by X-ray diffraction, Figure S1. SEM inspection highlights a uniform mass of aggregated particles, Figure S2; at higher magnification, the grain-like structure of the particles building the aggregates appears. More information on the size and morphology of the embryonic

https://dx.doi.org/10.1021/acs.chemmater.9b05258
Chem. Mater. XXXX, XXX, XXX−XXX

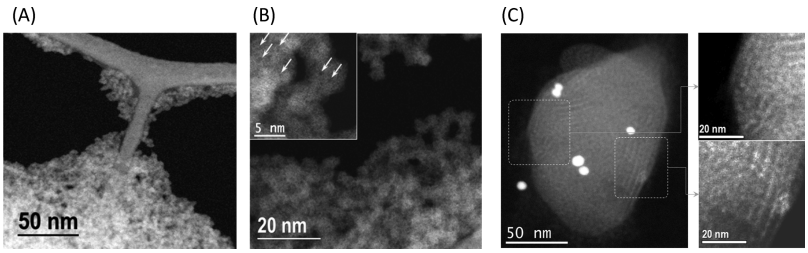

Figure 2. (A) Low- and (B) high-magnification views of the freeze-dried P_{RT}-TPA sample and (C left) colloidal crystal made of uniform-size P_{RT}-TPA zeolite embryos and (C right) a high-magnification view of the arrays of EZs building the colloidal crystals. Note: the white spots in the left image are gold particles employed for the alignments.

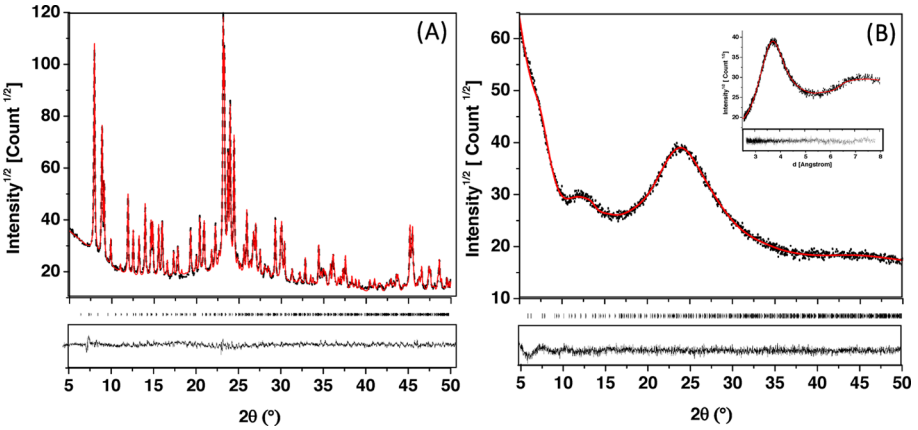

Figure 3. XRD diagrams and Rietveld fits for (A) well-crystallized (mean crystallite sizes are 133(10) nm; GoF = 1.9) and (B) embryonic samples (GoF = 1.2). Bottom diagrams are difference curves; the inset in (B) is plotted in the d-scale.

zeolites was obtained by STEM-HAADF. Upon freeze-drying, discrete particles are observed. Their size (3−5 nm) matches well the result of DLS analysis. The particles generally exhibit a spherical morphology with a rough surface most probably due to the presence of pores with diameters of <0.9 nm as indicated by the arrows in the inset of Figure 2B.

Upon slow evaporation at room temperature, colloidal formation with arrays of individual EZs similar in size can be identified, Figure 2C. The formation of a crystal-like entity from the EZ shows the uniform nature of the colloidal suspension obtained after the RT synthesis where only discrete particles of similar size are present. Besides, the agglomerates exhibit an area of short-range order with the spherical EZ as units.

Figure 3 shows the difference in XRD diagrams between fully crystallized and amorphous EZs prepared with TPA. While the fully crystallized powder (see Figure 3A) clearly exhibits narrow diffraction peaks with cell parameters coherent with the original structure (a = 2.00484(7) nm, b = 1.99267(6) nm, and c = 1.33919(5) nm), the amorphous sample (see Figure 3B) only gives rise to first- and second-order modulations due to the closest and second-closest neighboring atoms of the structure. We could fit this latter diagram using crystallite sizes typically of the order of the unit cell (typically a few nanometers) and significant microstrains (typically 0.05 rms) with slightly isotropized cell parameters (a = 1.906(6) nm, b = 1.70(2) nm, and c = 1.55(1) nm). Such fitted parameters are only helping the fit but could not represent the first significant contribution appearing below 2θ = 10°. This latter contribution is associated with the periodical arrangement of the embryos depicted by the electron density contrasts observed in TEM images (see Figure 2C) and cannot be modeled in the XRD diagrams using the Mobil Five (MFI)-type structure. We instead used a simple Gaussian background contribution to account for it in the Rietveld fits. As a result (see Figure 3B, inset), the first and second scattering contributions are located around 3.68 and 7.1 Å, respectively. In the MFI-type structure, such contributions characterize the mean distances between closest Si−O polyhedra with corresponding first and second scattering orders. The first distance at 3.68 Å is also close to the one observed in fumed silica of approximately 3.9 Å (see Figure S3A) while no periodicity is observed (see Figure S3B).

As X-ray diffraction is not the best technique to probe short-range orders, on such embryonic zeolites, we resorted to infrared spectroscopy (IR) to characterize the structure of ultrasmall zeolite embryos. The IR spectra display three main absorption bands around 1080 (with a shoulder at 1200 cm^{-1}), 800, and 460 cm^{-1}, Figure S4. The first two correspond to asymmetric and symmetric Si−O stretching motions and the last one to a bending Si−O−Si mode. A shoulder at 560 cm^{-1} is also observed and assigned to the bending vibrations of external Si−O.[36] The bands around 560 and 1200 cm^{-1} are generally attributed to the double-membered ring and external asymmetric stretching in the MFI structure, respectively,[37] while the optical density ratio of 560 and 460 cm^{-1} bands is commonly used to determine the zeolite crystallinity.[37] The crystallinities of the P_{RT}-TMA, P_{RT}-TPA, and P_{RT}-THA samples are similar according to such an IR study. The synthesized materials exhibit a type I isotherm with a significant uptake at low relative pressure followed by horizontal adsorption−desorption branches. A closer look at the isotherms reveals small differences between the material synthesized with TMA (P_{RT}-TMA) and larger templates. The

https://dx.doi.org/10.1021/acs.chemmater.9b05258
Chem. Mater. XXXX, XXX, XXX−XXX

isotherm of P_{RT}-TMA is of type Ia, characteristic of ultramicropores (<0.7 nm), whereas the others (TPA, TBA, TMAd, and THA) are of type Ib, characteristic of supermicropores (1−2.5 nm) according to the classification of IUPAC.[38] The latter isotherms show a much higher uptake indicative of larger micropore volumes. The isotherm of nanosized ZSM-5 is included in Figure 4, and the data derived from the isotherm are summarized in Table S1.

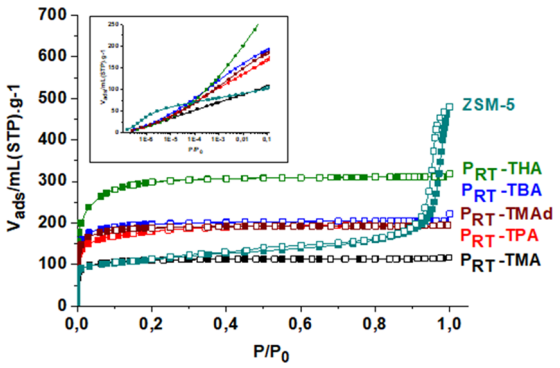

Figure 4. N_2 adsorption−desorption isotherms of P_{RT}-SDA samples where the SDA is TMA, TPA, TMAd, TBA, and THA. The isotherm of nanosized ZSM-5 is included as a benchmark. The inset is plotted in the logarithmic *x*-axis scale and represents the low (<0.1 P/P_0) pressure range.

The micropore volume of the MFI-type material is similar to that of P_{RT}-TMA and much lower than that of the embryos synthesized with larger templates. However, the total pore volume of the crystalline material is higher due to textural mesoporosity, revealed by the slope of the isotherm in the 0.2−0.8 pressure range and second uptake in the 0.9−1.0 range, between nanosized zeolite particles. Such a textural porosity is not present in the embryonic zeolites. If some textural pores exist, that is, pores between ultrasmall nanoparticles (3−4 nm) formed around the template, these pores remain in the microporous range.

The data summarized in Table S1 show that the microporous volume and specific surface area increase with the size of the SDA used. More precisely, V_{micro} and S_{BET} increase from 0.17 to 0.47 $cm^3 \cdot g^{-1}$ and from 418 to 1095 $m^2 \cdot g^{-1}$, respectively, for TMA and THA. A small increase in the micropore volume (TBA > TMAd > TPA) is noticeable.

In general, templates with approximately similar sizes yield materials with very close specific surface areas and micropore volumes; a close positive correlation between the size of the OSDA and V_{micro} and S_{BET} is indeed observed on these samples. It is well known that tetraalkylammonium cations play a key role in zeolite synthesis by ordering around them aluminosilicate species, akin to water clathrates, by progressive displacement of hydrogen-bound water molecules.[39−42] As long as synthesis is stopped before crystallization, the harvested materials are silica−alumina matrices organized around these OSDAs and form cages of different volumes depending on the size of the SDA used.

The pore size distributions and cumulative pore volumes of P_{RT}-TPA and P_{RT}-THA extracted by DFT using cylindrical geometry (model of a "N_2-cylindrical pore-oxide surface") are displayed in Figure S5. The EZ prepared with TPA has a wide distribution of pore widths ranging between 8 and 20 Å with the highest population of pores smaller than 14 Å; they correspond to a cumulative pore volume of 0.15 $cm^3 \cdot g^{-1}$. Moreover, the EZ prepared in the presence of THA does not contain pores with a size below 1 nm. The population of large pores (>14 Å) is most largely presented in this sample. Despite their higher V_{micro} and S_{BET}, no additional larger pores are observed, so pores larger than 14 Å dominate in this material. This is clear from the increase of their incremental volume and decrease of the cumulative pore volume of pores smaller than 14 Å from 0.15 to 0.09 $cm^3 \cdot g^{-1}$. Some textural pores represented by a large peak centered at approximately 27 Å, which are present in P_{RT}-TPA. These data unambiguously imply that the size of the OSDA determines the pore size of the embryonic zeolites; a smaller OSDA yields pores of smaller widths, while a larger OSDA leads to larger pores.

The pore structure of EZs can be studied by relating the confinement of Xe molecules to their chemical shift.[43] Low chemical shift peaks, close to 0 ppm, indicate large (meso-)pores, while high chemical shifts indicate more confined space (micro-)pores. The NMR spectra of HP ^{129}Xe adsorbed on the P_{RT}-TPA and P_{RT}-THA samples recorded at different temperatures are shown in Figure 5. In addition to the peak of xenon in the gas phase at 0 ppm, all spectra exhibit additional resonance, which differ for P_{RT}-TPA and P_{RT}-THA samples. The P_{RT}-TPA material exhibits a single peak (136−92 ppm) in the 200−320 K temperature range. The peak in the P_{RT}-THA sample shifts from 115 to 84 ppm in the 200−320 K temperature range. The higher chemical shift of Xe adsorbed in P_{RT}-TPA can be attributed to xenon atoms located in a more confined environment. This result is in good agreement with the physisorption measurements showing that the large THA template generated EZs with a substantially higher pore volume.

In order to gain more insight into the structure and properties of the embryonic zeolites, the samples are further characterized by thermal analysis (TG/DSC, Figure S6) and

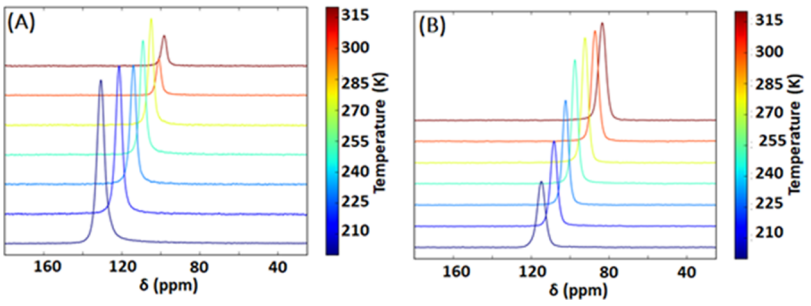

Figure 5. NMR Spectra of HP ^{129}Xe adsorbed on (A) P_{RT}-TPA and (B) P_{RT}-THA samples recorded at variable temperature (200-320 K).

https://dx.doi.org/10.1021/acs.chemmater.9b05258
Chem. Mater. XXXX, XXX, XXX−XXX

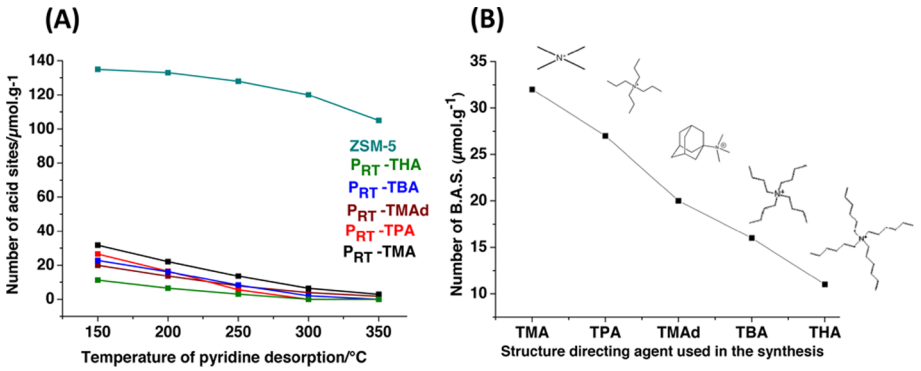

Figure 6. Number of Brønsted acid sites (μmol·g^{-1}) for P_{RT}-OSDA and nanosized ZSM-5 at different temperatures determined by (A) TPD of pyridine and (B) at 150 °C as a function of OSDA size.

^{13}C CP MAS NMR spectroscopy, Figure S7.[44] Prior to TG analyses, the samples are equilibrated overnight under a 79% relative humidity at room temperature. The thermograms of different samples are fairly similar to two well-established regions: first, between room temperature and 200−250 °C and, second, between 250 and 500 °C. The weight loss below 200 °C is associated with an endothermic peak and attributed to water release. The weight loss at higher temperature (250−500 °C) is associated with an exotherm (DSC) and corresponds to the OSDA oxidation. Compared to a crystalline zeolitic material, the embryonic zeolites are much more hydrophilic. For instance, the water content of ZSM-5 is approximately 5%, while its amorphous counterpart synthesized with TPA contains approximately 35 wt % water. It is worth noting that the water content increases with the increasing size of the OSDA used from 38 to 48 and 52% with TMA, TPA, and THA, respectively. Most of the water is released at approximately 60 °C on P_{RT}-THA and at higher temperatures on samples containing smaller structure-directing agents (P_{RT}-TPA and P_{RT}-TMA); this further implies that larger (hydrated) OSDAs lead to embryos with more open structures. The OSDA oxidation includes several steps: one common around 280−300 °C, characteristic of weakly bound cations located on the external surface of the embryonic units, and another at higher temperature related to the size of OSDA. With a smaller OSDA, its decomposition is slower due to confinement and more restricted access of the oxidant (O_2) highlighted by a shift to higher temperatures (450 °C in PTMA vs 350 °C in PTPA/THA).

^{13}C CP MAS NMR spectroscopy of the embryonic zeolites shows for each carbon frequency a superposition of a narrow signal and a large signal with a slight chemical shift. The narrow signals correspond to the OSDA in less restricted environments, most probably located on the external surface of zeolite embryos, while the larger ones correspond to the OSDA in more confined environments, the OSDA occluded into zeolite embryos, Figure S7. This is indicative of the OSDA in two different environments.[45] The first sharp one belongs to a mobile OSDA, most probably located on the external surface of zeolite embryos, while the second broader one corresponds to the OSDA located in a more confined space. This is consistent with the previously observed two exotherms on the DSC, namely, (i) 200−250 °C, the OSDA in a loosely confined environment, and (ii) 250−500 °C, the OSDA in a more confined environment. Moreover, the ^{13}C CP MAS NMR of TPA$^+$ occluded in crystalline ZSM-5 has the distinctive splitting of its C3 (terminal methyl) peak attributed to the presence of two different environments (linear and zigzag channels) in the zeolite channels.[46,47] Such a splitting is not observed in P_{RT}-TPA, indicating the presence of its methyl groups (C3) in a unique environment. A shift of −3 ppm of the C1 peak in the EZ indicates a more distorted angular configuration of its methylene group attached to the nitrogen as reported earlier.[48]

Figure S8A shows the ^{27}Al NMR spectra of all as-prepared samples with a single peak centered at 53 ppm, characteristic of tetrahedral aluminum. After calcination, Figure S8B, aluminum is present in other coordinations: a majority remains in the tetrahedral coordination (ca. 53 ppm), some become octahedral (between 0 and -40 ppm), and a broad peak (between 0 and 30 ppm) appearing often to be attributed to distorted tetrahedral Al and/or penta-coordinated Al can be observed. The proportion of nontetrahedral Al varies in the different samples. By deconvoluting the spectra using the Dmfit program, the relative fraction of octahedral aluminum is estimated between 38% (P_{RT}-TMA) and 26% (P_{RT}-THA), higher than the 10% usually observed for a pentasil-type zeolite. However, this amount is substantially lower than what is observed in a variety of amorphous aluminosilicates.[49] This indicates that a substantial portion of Al is stabilized in a silica matrix and remains there upon calcination at high temperature. The dealumination of zeolites depends on both the framework type and the T site within a given zeolite.[50,51] The larger proportion of octahedral Al is observed in the calcined P_{RT}-TMA embryos and the lowest in P_{RT}-THA; this could be related to the bond angles of the alumina-silica species surrounding the template, as the small TMA generates an inorganic network with more stress than the larger templates.

The acidity of embryonic samples is characterized by in situ infrared spectroscopy using pyridine as a probe molecule. The number of Brønsted acid sites (BAS) is calculated from the pyridinium band at 1545 cm^{-1} after the evacuation of pyridine at different desorption temperatures. The results are given in Figure 6.

The embryonic zeolites possess a significantly lower concentration (<40 μmol·g^{-1}) and strength of Brønsted acid sites in comparison to ZSM-5 (~135 μmol·g^{-1}), attributed to a wider distribution of angular configurations and organization of the alumino-silicate matrix compared to highly crystalline zeolites. After pyridine desorption at 150 °C, the embryonic zeolites have slightly different concentrations of BAS, depending on the employed OSDA. A smaller OSDA leads to higher BAS concentrations (Figure 6B). An increase in the size/charge ratio of an OSDA leading to a decrease in the number

https://dx.doi.org/10.1021/acs.chemmater.9b05258
Chem. Mater. XXXX, XXX, XXX−XXX

Table 1. Number of Brønsted Acid Sites (μmol·g^{-1}) of P-OSDA Prepared at RT and 90 °C

	embryonic samples												
	P-TMA		P-TPA			P-TMAd			P-TBA		P-THA		ZSM-5
temperature	RT	$P_{90\text{-}15}$	RT	$P_{90\text{-}15}$	$P_{90\text{-}18}$	RT	$P_{90\text{-}15}$	$P_{90\text{-}216}$	$P_{90\text{-}15}$	$P_{90\text{-}144}$	RT	$P_{90\text{-}144}$	$P_{100\text{-}48}$
150	32	34	27	35	38	20	40	37	23	20	11	22	135
200	22	23	17	27	29	14	27	26	16	15	7	15	133
250	14	12	6	18	18	8	15	15	8	7	3	7	128
300	6	5	0	8	9	4	5	6	2	0	0	0	120
350	3	1	0	2	2	2	2	1	0	0	0	0	105

of BAS was already reported by Barrer and Denny,[52] Aeillo and Barrer,[53] and Kerr[54] for different zeolites. After desorption at a higher temperature (>250 °C), the number of Brønsted acid sites is close to zero for all samples, indicative of the low acid strength of the embryonic zeolites. By combining ICP analysis and ^{27}Al NMR results, it is possible to evaluate the amount of Al^{IV} in each sample and therefore the number of expected BASs. The pyridine method accounts, however, for only 20% of the expected amount of BASs. This might be due to the presence of BASs in a very confined environment inaccessible to pyridine or the fact that the remaining Al^{IV} present in the calcined samples does not completely correspond to BASs. Indeed, the peak centered at 53 ppm in ^{27}Al NMR is not symmetrical and presents an extension between 40 and 10 ppm, which can be attributed to highly distorted, tetrahedral, nonframework aluminum−oxygen species. The chemical shift around 30 ppm is also consistent with penta-coordinated aluminum.[55,56] In addition, during calcination, the tetrahedral symmetry of the lattice aluminum must be lost, and aluminum species of low symmetry are formed. In a low-symmetry environment, aluminum can become "invisible" due to important peak broadening of this quadrupolar nucleus.[57−59]

The accessibility to active sites (BAS) is best studied by infrared spectroscopy of adsorbed probe molecules of different kinetic diameters, namely, pyridine (0.57 nm) and collidine (0.74 nm).[35] The results of such experiments performed under similar conditions are summarized in Figure S9. The number of BASs is calculated from the bands associated with protonated pyridine (1545 cm^{-1}) and collidine (1648 cm^{-1}) after the adsorption and evacuation of the physisorbed portion of the adsorbates. The accessibility to the BAS is defined as the ratio between the number of BASs measured by collidine and pyridine. While, with TMA OSDA (P_{RT}-TMA), the accessibility is 0.37, that is, the sites probed by collidine are less than half of those probed by pyridine (13 μmol·g^{-1} vs 36 μmol·g^{-1}), it becomes 1 when TPA is the OSDA (P_{RT}-TPA). This indicates that all active sites are accessible to both molecules in the latter. Therefore, in the presence of small OSDAs, small pores are formed, restricting accessibility of their Brønsted acid sites to bulky molecules and leading to potential shape-selective effects in embryonic zeolites.

^{29}Si NMR spectra of as-synthesized and calcined embryonic zeolites prepared in the presence of the smallest (TMA), medium (TPA), and largest (THA) OSDAs show different silicon environments, Q^2, Q^3, and Q^4 (Figure S10).[60] Their deconvolution with the Dmfit program gives the relative fraction of each species. After calcination, the chemical shifts are unchanged, but the relative areas of Q^2 and Q^3 decrease while those of Q^4 increase. These changes result from two simultaneous events upon heating: (i) some tetrahedral Al changing coordination and (ii) condensation of some silica species. The calcined samples have almost the same ratio of Q^3 and Q^4 species, but the contribution of Al and OH groups to the Q^3 species differs between different samples.

Impact of Temperature and Synthesis Time on the Physicochemical Properties of Embryonic Zeolites. In addition to room-temperature synthesis, embryonic zeolites are prepared at 90 °C for 12−216 h. As for the RT syntheses, all samples are freeze-dried before further processing and characterization.

The synthesis time is carefully controlled to obtain preformed units with only a short-range order. Only the system containing TPA yields a crystalline phase (MFI-type) in syntheses longer than 24 h. The other systems are always amorphous after crystallization up to 216 h (Figure S11).

The ^{13}C CP MAS NMR of the TMA, TPA, and THA templates and the embryonic zeolites synthesized at RT and 90 °C are displayed in Figure S7. All characteristic peaks of the template are present in the spectra of the embryonic zeolites. Peak broadening, an indication of the presence of the template in a confined environment, is observed.

Like the embryonic zeolites obtained at RT, the solids synthesized at 90 °C exhibit a type I adsorption isotherm characteristic of a microporous material. In general, the materials synthesized at 90 °C show an increase in nitrogen uptake with respect to their counterpart obtained at RT, Figure S12. This suggests a better structuring of these embryonic zeolites. The maximum micropore volume is achieved after different synthesis times for different templates. For instance, it is 12 h for a TPA synthesis and it decreases after 18 h, Figure S12B; this is related to the onset of crystallization of MFI. With TBA, there is no difference between 15 and 144 h, Figure S12C, while with TMAd, the micropore volume increases up to 216 h of hydrothermal synthesis. The single exception is with THA where the 90 °C synthesis shows a lower pore volume and surface area (0.38 cm^3·g^{-1} and 911 cm^2·g^{-1}) than those of its RT counterpart (0.47 cm^3·g^{-1} and 1095 cm^2·g^{-1}), Figure S12E and Table S2. It is difficult to determine the reason for such a trend, but it could be related to the large size of the THA molecule and a more efficient condensation of the aluminosilicate species at a higher temperature.

The effect of synthesis temperature on the state of Al in the embryonic zeolites is investigated by ^{27}Al MAS NMR and IR-monitored pyridine desorption. The ^{27}Al MAS NMR spectra of all as-synthesized samples exhibit a single peak (ca. 53 ppm) indicating the sole presence of tetrahedral aluminum, Figure S13. However, after calcination at 550 °C, the intensity of this peak decreases, indicating that a portion of aluminum leaves its tetrahedral coordination. At the same time, two peaks emerge: a sharp and small one at 0 ppm, typical for octahedrally coordinated aluminum, and a broad one between 0 and −30 ppm, attributed to the presence of different polymorphs of aluminum. Deconvolution of these spectra with the Dmfit program can evaluate the amount of nontetrahedral aluminum.

https://dx.doi.org/10.1021/acs.chemmater.9b05258
Chem. Mater. XXXX, XXX, XXX−XXX

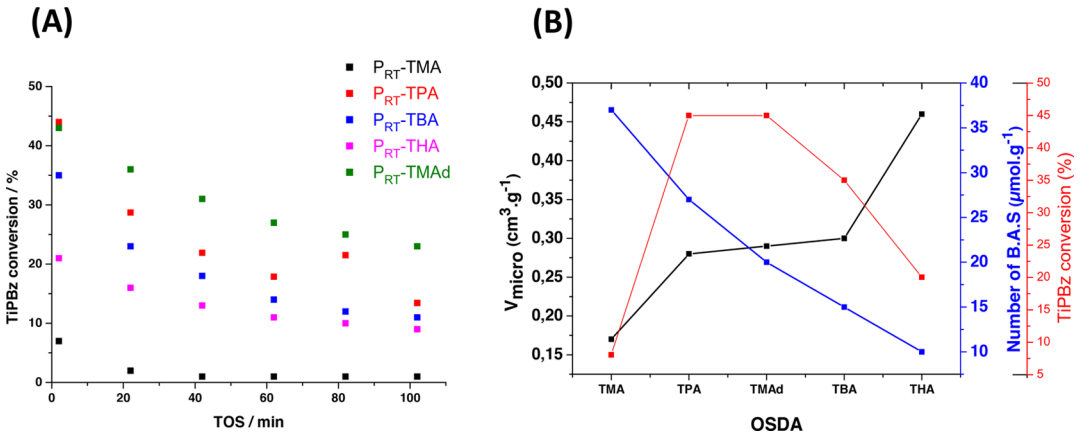

Figure 7. (A) TiPBz conversion of RT synthesized embryonic zeolites. (B) TiPBz conversion, number of Brønsted acid sites, and micropore volume of the embryonic zeolites as a function of the OSDA in the synthesis. Catalytic test conditions: T = 300 °C, WHSV = 8 h^{-1}, and TOS = 2 min.

The octahedral aluminum content decreases in the 90 °C synthesis. The tetrahedral aluminum peak (53 ppm) is not symmetrical in all samples and tails between 40 and 10 ppm. As mentioned above, this can be attributed to the presence of highly distorted, tetrahedral, nonframework aluminum−oxygen species or penta-coordinate aluminum.

IR spectroscopy of adsorbed pyridine measures the acidity of the embryonic zeolites. The number of Brønsted acid sites calculated from the pyridinium ion band (1545 cm^{-1}) are summarized in Table 1.

The acidity of the EZ prepared at 90 °C increases with synthesis time, but differences are marginal. As for the room-temperature EZ syntheses, the smaller the OSDA, the higher the number of BASs; differences, however, are not substantial, and all EZs possess a much lower number of acid sites than that of ZSM-5 with a similar Si/Al ratio.

Catalytic Activity. Earlier studies showed amorphous zeolite precursors compelling catalytic performances in hydrocarbon conversion.[61,62] In the present work, we evaluated the catalytic performances of embryonic zeolites prepared at RT in the dealkylation of triisopropylbenzene (TiPBz), Figure 7A. Its kinetic diameter (0.95 nm) is well above the pore openings of the MFI-type zeolite (0.56 nm), and TiPBz is therefore commonly used to study the external surface properties of zeolites, including the large-pore (12 Membered Ring (MR)) ones.

P_{RT}-TMAd and P_{RT}-TMA EZs lead to the highest and lowest conversions, respectively, Figure 7A. Figure 7B highlights the effects of the OSDA on the conversion, number of Brønsted acid sites, and micropore volume. While P_{RT}-TMA possesses the highest number of Brønsted acid sites, the smallest conversion of TiPBz is related to the limited accessibility of its acid sites. This clearly indicates that the OSDA size is a tool to control the size selectivity of the EZ. For instance, TPA- and TMAd-generated materials comprise relatively strong Brønsted acid sites in micropores large enough to process TiPBz. Conversely, the larger TBA and THA OSDAs generate EZs with larger micropores accessible to bulky molecules, but their catalytic performances are low due to a lack of Brønsted acid sites. Thus, EZs combining a critical number of active sites with pores opening large enough to transport the bulky TiPBZ display the best catalytic performances; the catalytic properties of embryonic zeolites can be tuned by accessibility and acid/active site density.

CONCLUSIONS

X-ray amorphous zeolite precursors, the so-called embryonic zeolites (EZ), are prepared with OSDAs identical to those used in the synthesis of conventional zeolites. The synthesis conditions need to be controlled to obtain monodisperse suspensions of zeolite precursor particles with a size of a few nanometers. Thorough physicochemical characterization indicates that such zeolite precursors are highly uniform, and their properties strongly depend on the template used. All are microporous materials as the majority of their pores are in the range of 1−2 nm. Some exhibit impressive specific surface areas (1095 $cm^2 \cdot g^{-1}$) and micropore volumes (0.47 $cm^3 \cdot g^{-1}$), larger than that of zeolites obtained with the same template. They are stable upon calcination and can be used as heterogeneous catalysts. While they possess a relatively low number of active sites of moderate acid strength, they display high activity in bulky-molecule conversion as their performance depends on and can be tuned by controlling their acidity and the accessibility of their active sites. EZs, therefore, extend the range of applications of current zeolites especially for bulky molecules; these are encountered in the processing of heavy oil fractions and biomass.

ASSOCIATED CONTENT

Supporting Information

The Supporting Information is available free of charge at https://pubs.acs.org/doi/10.1021/acs.chemmater.9b05258.

Characterization data: XRD, SEM, FTIR, N_2 adsorption−desorption, pore size distribution (DFT calculation), TG/DSC, and NMR (PDF)

AUTHOR INFORMATION

Corresponding Author

Valentin Valtchev − *Normandie Univ, ENSICAEN, UNICAEN, CNRS, Laboratoire Catalyse et Spectrochimie, 14050 Caen, France;* orcid.org/0000-0002-2341-6397; Email: valentin.valtchev@ensicaen.fr

Authors

Mariame Akouche − *Normandie Univ, ENSICAEN, UNICAEN, CNRS, Laboratoire Catalyse et Spectrochimie, 14050 Caen, France;* orcid.org/0000-0003-0490-7825

https://dx.doi.org/10.1021/acs.chemmater.9b05258
Chem. Mater. XXXX, XXX, XXX−XXX

Jean-Pierre Gilson − *Normandie Univ, ENSICAEN, UNICAEN, CNRS, Laboratoire Catalyse et Spectrochimie, 14050 Caen, France;* orcid.org/0000-0002-3543-8163
Nikolai Nesterenko − *Total Research and Technology Feluy (TRTF), 7181 Feluy, Belgium*
Simona Moldovan − *Institut des Sciences Appliquées de Rouen, Groupe de Physique des Matériaux (GPM), Rouen University, 76801 Rouen, France*
Daniel Chateigner − *Normandie Univ, ENSICAEN, UNICAEN, CNRS, Laboratoire de Cristallographie et Science des Matériaux, 14050 Caen, France*
Hussein El Siblani − *Normandie Univ, ENSICAEN, UNICAEN, CNRS, Laboratoire Catalyse et Spectrochimie, 14050 Caen, France*
Delphine Minoux − *Total Research and Technology Feluy (TRTF), 7181 Feluy, Belgium*
Jean-Pierre Dath − *Total Research and Technology Feluy (TRTF), 7181 Feluy, Belgium*

Complete contact information is available at: https://pubs.acs.org/10.1021/acs.chemmater.9b05258

Author Contributions

All authors have given approval to the final version of the manuscript.

Funding

This research was supported by TOTAL Raffinage Marketing and the Industrial Chair ANR-TOTAL "Nanoclean Energy".

Notes

The authors declare no competing financial interest.

■ ACKNOWLEDGMENTS

The financial support was from TOTAL Raffinage Marketing and the Industrial Chair ANR-TOTAL "Nanoclean Energy". V.V. and S.M. acknowledge the financial support from CARNOT-ESP 3DNANOZET 5281. GENESIS is supported by the Région Haute-Normandie, Métropole Rouen Normandie, CNRS via LABEX EMC, and the French National Research Agency as a part of the program "Investissements d'avenir" with reference no. ANR-11-EQPX-0020. The authors appreciate the technical support of Marie Desmurs.

■ REFERENCES

(1) Flanigen, E. M.; Broach, R. W.; Wilson, S. T. *In Zeolites in Industrial Separation and Catalysis*; Kulprathipanja, S. Ed.; Wiley-VCH: Weinheim, Germany, 2010; pp 1−26.
(2) Bellussi, G.; Carati, A.; Millini, R. In *Zeolites and Catalysis:Synthesis, Reactions and Applications*; Cejka, J., Corma, A., Zones, S. Eds.; Wiley-VCH: Weinheim, Germany, 2010; pp 449−491.
(3) Marcilly, C. R. Where and how shape selectivity of molecular sieves operates in refining and petrochemistry catalytic processes. *Top. Catal.* **2000**, *13*, 357−366.
(4) Vermeiren, W.; Gilson, J.-P. Impact of zeolites on the petroleum and petrochemical industry. *Top. Catal.* **2009**, *52*, 1131−1161.
(5) Martínez, C.; Corma, A. Inorganic molecular sieves: Preparation, modification and industrial application in catalytic processes. *Coord. Chem. Rev.* **2011**, *255*, 1558−1580.
(6) Landau, M. V.; Vradman, L.; Valtchev, V.; Lezervant, J.; Liubich, E.; Talianker, M. Hydrocracking of heavy vacuum gas oil with a Pt/H-beta− Al2O3 catalyst: effect of zeolite crystal size in the nanoscale range. *Ind. Eng. Chem. Res.* **2003**, *42*, 2773−2782.
(7) Corma, A.; Fornes, V.; Pergher, S.; Maesen, T. L.; Buglass, J. Delaminated zeolite precursors as selective acidic catalysts. *Nature* **1998**, *396*, 353.
(8) Vuong, G.-T.; Do, T.-O. A new route for the synthesis of uniform nanozeolites with hydrophobic external surface in organic solvent medium. *J. Am. Chem. Soc.* **2007**, *129*, 3810−3811.
(9) Choi, M.; Na, K.; Kim, J.; Sakamoto, Y.; Terasaki, O.; Ryoo, R. Stable single-unit-cell nanosheets of zeolite MFI as active and long-lived catalysts. *Nature* **2009**, *461*, 246.
(10) Tsapatsis, M.; Fan, W. A New, Yet Familiar, Lamellar Zeolite. *ChemCatChem* **2010**, *2*, 246−248.
(11) Smaïhi, M.; Gavilan, E.; Durand, J.-O.; Valtchev, V. P. Colloidal functionalized calcined zeolite nanocrystals. *J. Mater. Chem.* **2004**, *14*, 1347−1351.
(12) Xu, D.; Abdelrahman, O.; Ahn, S. H.; Guefrachi, Y.; Kuznetsov, A.; Ren, L.; Hwang, S.; Khaleel, M.; Al Hassan, S.; Liu, D. A quantitative study of the structure−activity relationship in hierarchical zeolites using liquid-phase reactions. *AIChE J.* **2019**, *65*, 1067−1075.
(13) Chal, R.; Gérardin, C.; Bulut, M.; Van Donk, S. Overview and industrial assessment of synthesis strategies towards zeolites with mesopores. *ChemCatChem* **2011**, *3*, 67−81.
(14) Perez-Ramirez, J.; Christensen, C. H.; Egeblad, K.; Christensen, C. H.; Groen, J. C. Hierarchical zeolites: enhanced utilisation of microporous crystals in catalysis by advances in materials design. *Chem. Soc. Rev.* **2008**, *37*, 2530−2542.
(15) Valtchev, V.; Majano, G.; Mintova, S.; Pérez-Ramírez, J. Tailored crystalline microporous materials by post-synthesis modification. *Chem. Soc. Rev.* **2013**, *42*, 263−290.
(16) Wei, Y.; Parmentier, T. E.; de Jong, K. P.; Zečević, J. Tailoring and visualizing the pore architecture of hierarchical zeolites. *Chem. Soc. Rev.* **2015**, *44*, 7234−7261.
(17) Valtchev, V.; Balanzat, E.; Mavrodinova, V.; Diaz, I.; El Fallah, J.; Goupil, J.-M. High energy ion irradiation-induced ordered macropores in zeolite crystals. *J. Am. Chem. Soc.* **2011**, *133*, 18950−18956.
(18) Haw, K.-G.; Gilson, J.-P.; Nesterenko, N.; Akouche, M.; El Siblani, H.; Goupil, J.-M.; Rigaud, B.; Minoux, D.; Dath, J.-P.; Valtchev, V. Supported Embryonic Zeolites and their Use to Process Bulky Molecules. *ACS Catal.* **2018**, *8*, 8199−8212.
(19) Jiang, J.; Yu, J.; Corma, A. Extra-large-pore zeolites: bridging the gap between micro and mesoporous structures. *Angewandte Chemie International Edition* **2010**, *49*, 3120−3145.
(20) Manton, M. R.; Davidtz, J. C. Controlled pore sizes and active site spacings determining selectivity in amorphous silica-alumina catalysts. *J. Catal.* **1979**, *60*, 156−166.
(21) Corma, A.; Pérez-Pariente, J.; Fornés, V.; Rey, F.; Rawlence, D. Synthesis and characterization of silica-alumina prepared from tetraalkylammonium hydroxides. *Appl. Catal.* **1990**, *63*, 145−164.
(22) Camblor, M. A.; Corell, C.; Corma, A.; Díaz-Cabañas, M.-J.; Nicolopoulos, S.; González-Calbet, J. M.; Vallet-Regí, M. A new microporous polymorph of silica isomorphous to zeolite MCM-22. *Chem. Mater.* **1996**, *8*, 2415−2417.
(23) Cantín, A.; Corma, A.; Diaz-Cabanas, M. J.; Jordá, J. L.; Moliner, M. Rational design and HT techniques allow the synthesis of new IWR zeolite polymorphs. *J. Am. Chem. Soc.* **2006**, *128*, 4216−4217.
(24) Liu, Z.; Ohsuna, T.; Terasaki, O.; Camblor, M. A.; Diaz-Cabañas, M.-J.; Hiraga, K. The first zeolite with three-dimensional intersecting straight-channel system of 12-membered rings. *J. Am. Chem. Soc.* **2001**, *123*, 5370−5371.
(25) Szostak, R. *In Handbook of molecular sieves: structures*; Springer Science & Business Media: New-York, 1992.
(26) Peng, C.; Liu, Z.; Yonezawa, Y.; Linares, N.; Yanaba, Y.; Trujillo, C. A.; Okubo, T.; Matsumoto, T.; García-Martínez, J.; Wakihara, T. Testing the limits of zeolite structural flexibility: ultrafast introduction of mesoporosity in zeolites. *J. Mater. Chem. A* **2020**, *8*, 735−742.
(27) S-Aguiar, E. F.; Murta-Valle, M.; Sobrinho, E.; Cardoso, D. Cracking of 1, 3, 5-triisopropylbenzene over deeply dealuminated Y zeolite. In *Studies in Surface Science and Catalysis*, Elsevier:, 1995, pp 417−422.

(28) Chateigner, D. Ed. *In Combined Analysis: Structure-texture-microstructure-phase-stresses-reflectivity analysis by X-ray and neutron scattering*, Wiley-ISTE: France, 2010 p 496.
(29) Lutterotti, L. Total pattern fitting for the combined size−strain−stress−texture determination in thin film diffraction. *Nuclear Instruments and Methods in Physics Research Section B: Beam Interactions with Materials and Atoms* **2010**, *268*, 334−340.
(30) Rietveld, H. A profile refinement method for nuclear and magnetic structures. *J. Appl. Crystallogr.* **1969**, *2*, 65−71.
(31) Popa, N. The (hkl) dependence of diffraction-line broadening caused by strain and size for all Laue groups in Rietveld refinement. *J. Appl. Crystallogr.* **1998**, *31*, 176−180.
(32) Gražulis, S.; Chateigner, D.; Downs, R. T.; Yokochi, A.; Quirós, M.; Lutterotti, L.; Manakova, E.; Butkus, J.; Moeck, P.; Le Bail, A. Crystallography Open Database−an open-access collection of crystal structures. *J. Appl. Crystallogr.* **2009**, *42*, 726−729.
(33) Happer, W. Optical pumping. *Rev. Mod. Phys.* **1972**, *44*, 169.
(34) Happer, W.; Miron, E.; Schaefer, S.; Schreiber, D.; Van Wijngaarden, W.; Zeng, X. Polarization of the nuclear spins of noble-gas atoms by spin exchange with optically pumped alkali-metal atoms. *Phys. Rev. A* **1984**, *29*, 3092.
(35) Nesterenko, N.; Thibault-Starzyk, F.; Montouilliout, V.; Yushchenko, V.; Fernandez, C.; Gilson, J.-P.; Fajula, F.; Ivanova, I. The use of the consecutive adsorption of pyridine bases and carbon monoxide in the IR spectroscopic study of the accessibility of acid sites in microporous/mesoporous materials. *Kinet. Catal.* **2006**, *47*, 40−48.
(36) Pichat, P.; Franco-Parra, C.; Barthomeuf, D. Infra-red structural study of various type L zeolites. *J. Chem. Soc., Faraday Trans. 1* **1975**, *71*, 991−996.
(37) Jansen, J.; Van der Gaag, F.; Van Bekkum, H. Identification of ZSM-type and other 5-ring containing zeolites by ir spectroscopy. *Zeolites* **1984**, *4*, 369−372.
(38) Thommes, M.; Kaneko, K.; Neimark, A. V.; Olivier, J. P.; Rodriguez-Reinoso, F.; Rouquerol, J.; Sing, K. S. Physisorption of gases, with special reference to the evaluation of surface area and pore size distribution (IUPAC Technical Report). *Pure Appl. Chem.* **2015**, *87*, 1051−1069.
(39) Derouane, E. G.; Determmerie, S.; Gabelica, Z.; Blom, N. Synthesis and characterization of ZSM-5 type zeolites I. physico-chemical properties of precursors and intermediates. *Appl. Catal.* **1981**, *1*, 201−224.
(40) Gittleman, C.; Bell, A.; Radke, C. Role of tetrapropylammonium cations in gel-phase silicalite synthesis. *Microporous Mater.* **1994**, *2*, 145−158.
(41) Corma, A.; Díaz-Cabañas, M. J.; Martínez-Triguero, J.; Rey, F.; Rius, J. A large-cavity zeolite with wide pore windows and potential as an oil refining catalyst. *Nature* **2002**, *418*, 514.
(42) Corma, A.; Díaz-Cabañas, M. J.; Rey, F.; Nicolopoulus, S.; Boulahya, K. ITQ-15: The first ultralarge pore zeolite with a bi-directional pore system formed by intersecting 14-and 12-ring channels, and its catalytic implications. *Chem. Commun.* **2004**, 1356−1357.
(43) Chen, F.; Chen, C.-L.; Ding, S.; Yue, Y.; Ye, C.; Deng, F. A new approach to determination of micropore size by 129Xe NMR spectroscopy. *Chem. Phys. Lett.* **2004**, *383*, 309−313.
(44) Gabelica, Z.; Derouane, E.; Gilson, J.-P. The use of combined thermal analysis to study crystallization, pore structure, catalytic activity and deactivation of synthetic zeolites. *Clay Miner.* **1984**, *19*, 803−824.
(45) Gittleman, C.; Watanabe, K.; Bell, A.; Radke, C. A mechanistic study of the synthesis of zeolite SSZ-24. *Microporous Mater.* **1996**, *6*, 131−150.
(46) Boxhoorn, G.; van Santen, R. A.; van Erp, W. A.; Hays, G. R.; Huis, R. An investigation into the structure and position of organic bases in ZSM-5-type zeolites by high-resolution solid-state 13 C nmr spectroscopy. *J. Chem. Soc., Chem. Commun.* **1982**, 264−265.
(47) Nagy, J. B.; Gabelica, Z.; Derouane, E. G. Position and configuration of the guest organic molecules within the framework of the ZSM-5 and ZSM-11 zeolites. *Zeolites* **1983**, *3*, 43−49.
(48) Dib, E.; Gimenez, A.; Mineva, T.; Alonso, B. Preferential orientations of structure directing agents in zeolites. *Dalton Trans.* **2015**, *44*, 16680−16683.
(49) Welsha, L.; Gilson, J.-P.; Gattuso, M. High resolution 27Al NMR of amorphous silica-aluminas. *Appl. Catal.* **1985**, *15*, 327−331.
(50) Silaghi, M.-C.; Chizallet, C.; Petracovschi, E.; Kerber, T.; Sauer, J.; Raybaud, P. Regioselectivity of Al−O Bond Hydrolysis during Zeolites Dealumination Unified by Brønsted−Evans−Polanyi Relationship. *ACS Catal.* **2014**, *5*, 11−15.
(51) Karwacki, L.; de Winter, D. M.; Aramburo, L. R.; Lebbink, M. N.; Post, J. A.; Drury, M. R.; Weckhuysen, B. M. Architecture-dependent distribution of mesopores in steamed zeolite crystals as visualized by FIB-SEM tomography. *Angew. Chem., Int. Ed* **2011**, *50*, 1294−1298.
(52) Barrer, R.; Denny, P. 202. Hydrothermal chemistry of the silicates. Part X. A partial study of the field CaO−Al 2 O 3−SiO 2−H 2 O. *J. Chem. Soc.* **1961**, 983−1000.
(53) Aiello, R.; Barrer, R. Hydrothermal chemistry of silicates. Part XIV. Zeolite crystallisation in presence of mixed bases. *J. Chem. Soc. A* **1970**, 1470−1475.
(54) Kerr, G. T. Chemistry of crystalline aluminosilicates. II. The synthesis and properties of zeolite ZK-4. *Inorg. Chem.* **1966**, *5*, 1537−1539.
(55) Campbell, S. M.; Bibby, D. M.; Coddington, J. M.; Howe, R. F.; Meinhold, R. H. Dealumination of HZSM-5 zeolites: I. *J. Catal.* **1996**, *161*, 338−349.
(56) Gilson, J.-P.; Edwards, G. C.; Peters, A. W.; Rajagopalan, K.; Wormsbecher, R. F.; Roberie, T. G.; Shatlock, M. P. Penta-coordinated aluminium in zeolites and aluminosilicates. *J. Chem. Soc., Chem. Commun.* **1987**, 91−92.
(57) Klinowski, J.; Thomas, J.; Fyfe, C.; Gobbi, G. Monitoring of structural changes accompanying ultrastabilization of faujasitic zeolite catalysts. *Nature* **1982**, *296*, 533.
(58) Fyfe, C.; Gobbi, G.; Kennedy, G. Investigation of the conversion (dealumination) of ZSM-5 into silicalite by high-resolution solid-state silicon-29 and aluminum-27 MAS NMR spectroscopy. *J. Phys. Chem.* **1984**, *88*, 3248−3253.
(59) Maijanen, A.; Derouane, E. G.; Nagy, J. B. FT-IR and solid-state NMR investigation of surface hydroxyl groups on dealuminated ZSM-5. *Appl. Surf. Sci.* **1994**, *75*, 204−212.
(60) Boxhoorn, G.; Kortbeek, A.; Hays, G.; Alma, N. A high-resolution solid-state29 Si nmr study of ZSM—5 type zeolites. *Zeolites* **1984**, *4*, 15−21.
(61) Jacobs, P. A.; Derouane, E. G.; Weitkamp, J. Evidence for X-ray-amorphous zeolites. *J. Chem. Soc., Chem. Commun.* **1981**, 591−593.
(62) Bellussi, G.; Perego, C.; Carati, A.; Peratello, S.; Massara, E. P.; Perego, G. Amorphous mesoporous silica-alumina with controlled pore size as acid catalysts. *Stud. Surf. Sci. Catal.* **1994**, *84*, 85−92.

https://dx.doi.org/10.1021/acs.chemmater.9b05258
Chem. Mater. XXXX, XXX, XXX−XXX